THE JOURNAL OF PHYSICAL CHEMISTRY B
A JOURNAL OF THE AMERICAN CHEMICAL SOCIETY

pubs.acs.org/JPCB

Article

RNA Electrostatics: How Ribozymes Engineer Active Sites to Enable Catalysis

Şölen Ekesan, Erika McCarthy, David A. Case, and Darrin M. York*

Cite This: *J. Phys. Chem. B* 2022, 126, 5982−5990

Read Online

ACCESS | Metrics & More | Article Recommendations

ABSTRACT: Electrostatic interactions are fundamental to RNA structure and function, and intimately influenced by solvation and the ion atmosphere. RNA enzymes, or ribozymes, are catalytic RNAs that are able to enhance reaction rates over a million-fold, despite having only a limited repertoire of building blocks and available set of chemical functional groups. Ribozyme active sites usually occur at junctions where negatively charged helices come together, and in many cases leverage this strained electrostatic environment to recruit metal ions in solution that can assist in catalysis. Similar strategies have been implicated in related artificially engineered DNA enzymes. Herein, we apply Poisson−Boltzmann, 3D-RISM, and molecular simulations to study a set of metal-dependent small self-cleaving ribozymes (hammerhead, pistol, and Varkud satellite) as well as an artificially engineered DNAzyme (8−17) to examine electrostatic features and their relation to the recruitment of monovalent and divalent metal ions important for activity. We examine several fundamental roles for these ions that include: (1) structural integrity of the catalytically active state, (2) pK_a tuning of residues involved in acid−base catalysis, and (3) direct electrostatic stabilization of the transition state via Lewis acid catalysis. Taken together, these examples demonstrate how RNA electrostatics orchestrates the site-specific and territorial binding of metal ions to play important roles in catalysis.

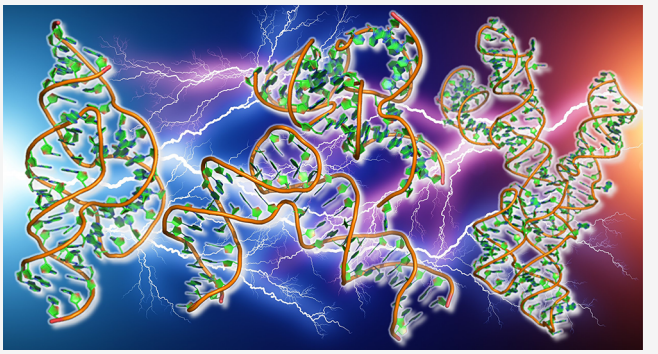

INTRODUCTION

Nucleic acid enzymes have been a subject of fascination since the first discovery of the catalytic properties of RNA more than three decades ago[1] and the first engineered DNA enzyme a decade later.[2] One intriguing question is how molecules of RNA (or DNA), with their limited repertoire of fairly inert building blocks, can fold into complex three-dimensional structures that form active site architectures able to recruit solvent components and promote catalysis. As will be discussed in this article, the origin of these remarkable capabilities are electrostatic in nature.

RNA electrostatics are central to structure and function.[3,4] RNA is built up from four elemental ribonucleotide bases, each of which carries a negative charge (under physiological conditions) along its phosphate backbone.[5] These charges are stabilized by the solvent environment and ion atmosphere[6,7] that typically contains both territorial and site-specific ion binding. Site-specific RNA binding occurs when cations (particularly divalent metal ions such as Mg^{2+}) bind tightly in a localized binding pocket. Territorial binding, on the other hand, occurs through delocalized cation accumulation and anion depletion in the vicinity of the nucleic acid, creating a neutralizing ion atmosphere.[8,9] Both site-specific and territorial binding can affect RNA structure and function. In RNA enzymes (ribozymes), this can occur through structural stabilization, pK_a tuning, or more direct chemical involvement as a general or Lewis acid.[10] The active sites of RNA enzymes occur at junctions[11]—structural elements that form when three or more helices come together. RNA junctions create a high localization of negative charge that typically requires binding of divalent metal ions in order to form under near-physiological ionic conditions. If found at the active site, these divalent metal ions may also play a direct or indirect chemical role in catalysis. It can thus be challenging to disentangle the specific role of metal ions in RNA folding and catalysis, as both are required for function.

This work explores how RNA electrostatics are used in ribozyme active sites to recruit monovalent and divalent metal ions that promote catalysis. The study of the solvation and ion atmosphere around nucleic acids, including enzymes,[12] has

Received: May 30, 2022
Revised: July 4, 2022
Published: July 21, 2022

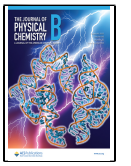

been a subject of great fundamental interest and research effort both experimentally[13] and computationally.[9,14] Experimental approaches have been reviewed,[7,15] and include so-called "ion counting" experiments,[16−18] anomalous small-angle X-ray scattering[19,20] and wide-angle X-ray scattering[21,22] and NMR.[23,24]

Here we consider four metal-dependent RNA-cleaving nucleic acid enzymes: the hammerhead (HHr), pistol (Psr), and Varkud satellite virus (VSr) ribozymes, and the 8−17 DNAzyme (8−17dz). The HHr, Psr, and VSr are naturally occurring small nucleolytic ribozymes,[25,26] whereas 8−17dz is an artificially engineered DNA enzyme.[27,28] These systems share a common L-platform/L-scaffold (L-P/S) design framework[29] and catalyze RNA strand cleavage, a reaction ubiquitous in biology,[10,30,31] via 2′-O transphosphorylation using a set of four fundamental catalytic strategies[10] illustrated in Figure 1. In this reaction, the 2′OH group of the RNA

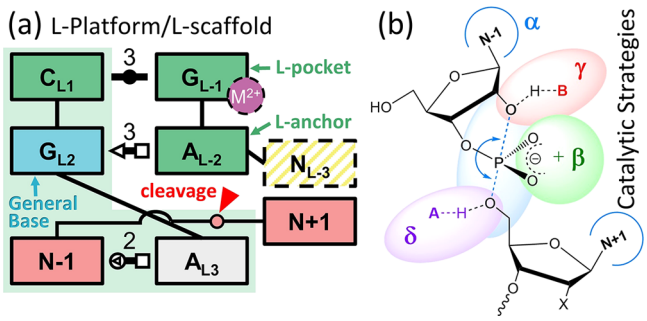

Figure 1. (a) L-platform/L-scaffold (L-P/S) design framework governing G+M and G+A classes of RNA cleaving nucleic acid enzymes. (b) Catalytic strategies[10] for RNA cleavage: α (blue) inline fitness, β (green) phosphate charge stabilization (for example, by a metal ion acting as a Lewis acid), γ (red) O2′ nucleophile activation (for example, by a general base), and δ (purple) O5′ leaving group stabilization (for example, by a general acid).

strand becomes activated by deprotonation facilitated by a general base, and carries out an inline nucleophilic attack to the adjacent scissile phosphate to proceed through a (presumably) dianionic pentavalent phosphorane transition state, followed by O5′ leaving group departure facilitated by a general acid to form a 2′,3′-cyclic phosphate product.

All these systems employ a conserved guanine (G) residue as the general base, and under near-physiological conditions, have a functionally important divalent metal ion (M) bound at the active site. In the HHr, Psr, and 8−17dz systems, the metal ion assists in general acid catalysis, and hence these systems are referred to as "G+M" nucleic acid enzymes[25] in reference to the participants in base and acid catalysis. The VSr, however, utilizes a conserved adenine as the general acid, and is thus referred to as a "G+A" ribozyme, and it has only been very recently that the structural and functional role of the active site metal ion has been identified.[32]

The remainder of the manuscript is organized as follows. The next section (Methods) describes details of the computational methods used. In the Results and Discussion section that follows, we initially consider the HHr, Psr and 8−17dz as members of the "G+M" classification. We first obtain a broad view of the electrostatic potential on the molecular (solvent excluding) surface from Poisson−Boltzmann (PB) calculations.[33−37] Next, we focus on the active site and use 3D reference interaction site model (3D-RISM) calculations[8,9,38−40] to characterize local electrostatics that lead to recruitment of monovalent ions at the Hoogsteen edge of the general base guanine and a divalent metal ion in the L-pocket. Next, we focus in further on the general base guanine itself, and use molecular dynamics (MD) simulations[41,42] to examine the radial distribution function of Na^+ ions around the O6 position enabling tuning of the pK_a. Finally, we present a case study of the VSr as an example of a "G+A" ribozyme. We illustrate how PB, 3D-RISM, and MD methods come together to predict a catalytically important Mg^{2+} binding in the active site, not apparent from X-ray crystallographic data, but was recently verified by biochemical experiments.[32] The identification of the functional role of the metal ion help to establish new connections between VSr and the "G+M" nucleic acid enzymes through an L-platform/L-scaffold (L-P/S) design framework[29] (Figure 1a). We conclude by tying these results together to establish how the fundamental underpinnings of these interrelations have their origins in biomolecular electrostatic phenomena.

METHODS

System Setup and MD Simulations. We have previously reported computational simulations for the HHr,[43] Psr,[44,45] 8−17dz,[46] and VSr[32] systems, and also made cross-cutting studies of the role of the divalent metal ion in promotion of productive hydrogen bonding of the O2′ nucleophile to facilitate its activation.[47] The details of the system setup, convergence of the simulations, and other specialized analysis can be found in these other works. Here, we identify and examine common electrostatic features and their relation to the recruitment of monovalent and divalent metal ions important for activity. We summarize the main distinguishing elements of the setup for each system, and refer the reader to the other works for full details.

The HHr system was built starting from the crystal structure with PDB ID2OEU.[48] The Mn^{2+} ions were replaced with Mg^{2+}. The GTP, OMC, and 5BU modified nucleobases were replaced with wild-type G, C, and U, respectively. The Psr system was built departing from the crystal structure with PDB ID 6R47.[49] Residue 33, reported as A in the PDB, was changed to G as is in the crystal sequence. The VSr and 8−17dz systems were built from their respective crystal structures (PDB ID: 5 V3I[50] for VSr and 5XM8[51] for 8−17dz). For all the systems, the nucleophile was not explicitly present in the crystal structure and was added based on internal coordinates of the sugar ring. Aside from their standard state (SS), where every residue is in its standard protonation state, each system was also setup with their corresponding general base guanine residues deprotonated at N1 position (GB^-), in order to sample the active state (AS) in solution ready to carry out the reaction. Systems were solvated with ions added to balance the system charge and achieve a bulk ion concentration of 0.14 M NaCl.

The solvated systems were equilibrated in a stepwise manner, following the protocol described in ref 46. Upon removal of all equilibration restraints, the systems were simulated for 100 ns in NPT ensembles, for overall system relaxation in solution. Stability (structure, energy, volume, and temperature fluctuations) and convergence (root-mean-square positional deviations of structures) were monitored, with convergence achieved around 50 ns.

All molecular dynamics (MD) simulations were carried out using AMBER20,[52] employing ff99OL3 RNA[53,54] and

https://doi.org/10.1021/acs.jpcb.2c03727
J. Phys. Chem. B 2022, 126, 5982−5990

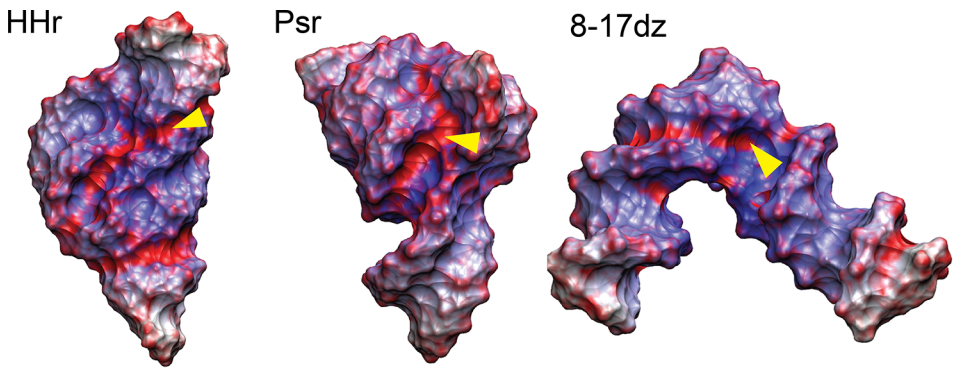

Figure 2. Electrostatic potential surfaces (EPS) projected on the molecular surfaces of HHr, Psr, and 8−17dz. EPS are obtained by Poisson−Boltzmann surface area (PBSA) calculations and visualized with probe radius of 3.0 Å. Negative, neutral, and positive charged regions of the EPS are depicted as red, white, and blue, respectively. The yellow triangles point toward the active site of the systems, which all present a prominently locally negative EPS.

ff99OL15 DNA[55] force field, TIP4P/Ew water model,[56] and corresponding Na^+/Cl^- ions[57] and 12−6−4[58] Mg^{2+} ions specifically tuned to have balanced interactions between solvent and nucleic acids.[59,60] The RNA force field has been reviewed and shown to be robust,[61] and the Mg^{2+} ion parameters are able to reproduce structural, thermodynamic, kinetic, and mass transport properties in bulk solution,[59] as well as experimental site specific binding free energies to nucleic acids derived from potentiometric pH titration data.[60]

Simulations were performed under periodic boundary conditions at 300 K using a 12 Å nonbond cutoff and particle mesh Ewald (PME) electrostatics.[62,63] The Langevin thermostat with $\gamma = 5\ ps^{-1}$ and Berendsen isotropic barostat with $\tau = 1$ ps were used to maintain a constant pressure and temperature. A 1 fs time step was used along with the SHAKE algorithm to fix hydrogen bond lengths,[64] with three-point SHAKE for the water molecules.[65] All production simulations were carried out in NPT ensembles.

Poisson−Boltzmann and 3D-RISM Calculations. Single point three-dimensional reference interaction site model (3D-RISM)[39,40] and Poisson−Boltzmann (PB)[33,34] calculations were performed with AMBER20[52] on representative active state structures from MD simultions stripped of solvent including metal ions. The *pbsa* solver[35−37] was used to output the spatial distribution of electrostatic potential for visualization in vmd with probe radius of 3.0 Å. The grid spacing for the finite difference PB solver was set at the default value of 0.5 Å, and the dielectric inferface was implemented with a level set function and the revised density function approach (ipb = 2, sasopt = 2). 3D-RISM calculations followed procedures similar to previous work.[8,9] DRISM calculations (32 768 grid points, 0.025 Å spacing) were first used to determine the site−site solvent susceptibilities required to perform 3D-RISM with the rism1d program. The modified direct inversion of the iterative subspace (MDIIS) approach was used to iteratively solve the DRISM equation with PSE2 closure to a residual tolerance of 10^{-12} at 298 K and a dielectric constant of 78.497 for bulk water. A constant density approach was used in which the denisty of water was assumed to to be 55.296 M with the addition of 10 mM Mg^{2+}, 140 mM Na^+, and 160 mM Cl^- using the SPC/E water model.[66] 3D-RISM was performed with rism3d.snglnt with PSE1 closure to a residual tolerance of 10^{-4} on a 232 × 232 × 232 $Å^3$ grid with a 116 × 116 × 116 $Å^3$ solventation box and without solvent−solvent interaction cutoff.

Radial Distribution of Na^+ around G:O6. Radial distribution functions were calculated from 500 ns trajectories for each system and state. The trajectories for 8−17dz were taken from previous work,[46] for standard state (SS) and general base deprotonated state (GB^-) with Pb^{2+} at the active site. Other trajectories were obtained from 5 independent runs initiating from 5 different starting points. The starting points were extracted from the initial 100 ns relaxation simulations starting from the 80 ns mark and taking frames 5 ns apart. Simulations from each starting point were run for 120 ns (total of 600 ns), the first 20 ns of which were discarded as equilibration, yielding 500 ns trajectories for analysis per system state, with frames saved every 10 ps.

Radial distribution functions (rdf) and coordination numbers (cn) of Na^+ around O6 of guanines were obtained using cpptraj,[67] with a bin size of 0.05 Å. Values for each guanine were calculated individually. The averages and their standard deviation were obtained excluding the results for the general base guanine.

RESULTS AND DISCUSSION

General Electrostatic Features of G+M Nucleic Acid Enzymes. We calculated electrostatic potential surface maps (EPS) for HHr, Psr, and 8−17dz systems using Poisson−Boltzmann solvent area (PBSA) approach. As illustrated in Figure 2, more prominent negative electrostatic potential (shown as red) can be seen in the grooves and helical junction. High local negative electrostatic potential is evident resulting from regions where the phosphates along the RNA backbone are in closest proximity. The active sites are located at the junction and indicated by yellow arrows in the figures. The local arrangement of phosphates in the active site, together with a guanine residue known as the "L-pocket" guanine,[29] forms a negatively charged "cage" that, as will be seen below, is essential for luring cations from solution into the active site to assist in catalysis.

Divalent Metal Ion Binding at the Active Site L-Pocket in G+M Nucleic Acid Enzymes. For the HHr, Psr, and 8−17dz "G+M" nucleic acid enzymes, we calculated the isodensity contour for Mg^{2+} and Na^+ ions separately using molecular solvation theory (3D-RISM). For each system, we used representative structures from equilibrated active states (that is, general base guanine activated by deprotonation at the N1) and removed all solvent and metal ions (that is, no explicit ions). We investigated the metal ion density 3D-RISM

https://doi.org/10.1021/acs.jpcb.2c03727
J. Phys. Chem. B 2022, 126, 5982−5990

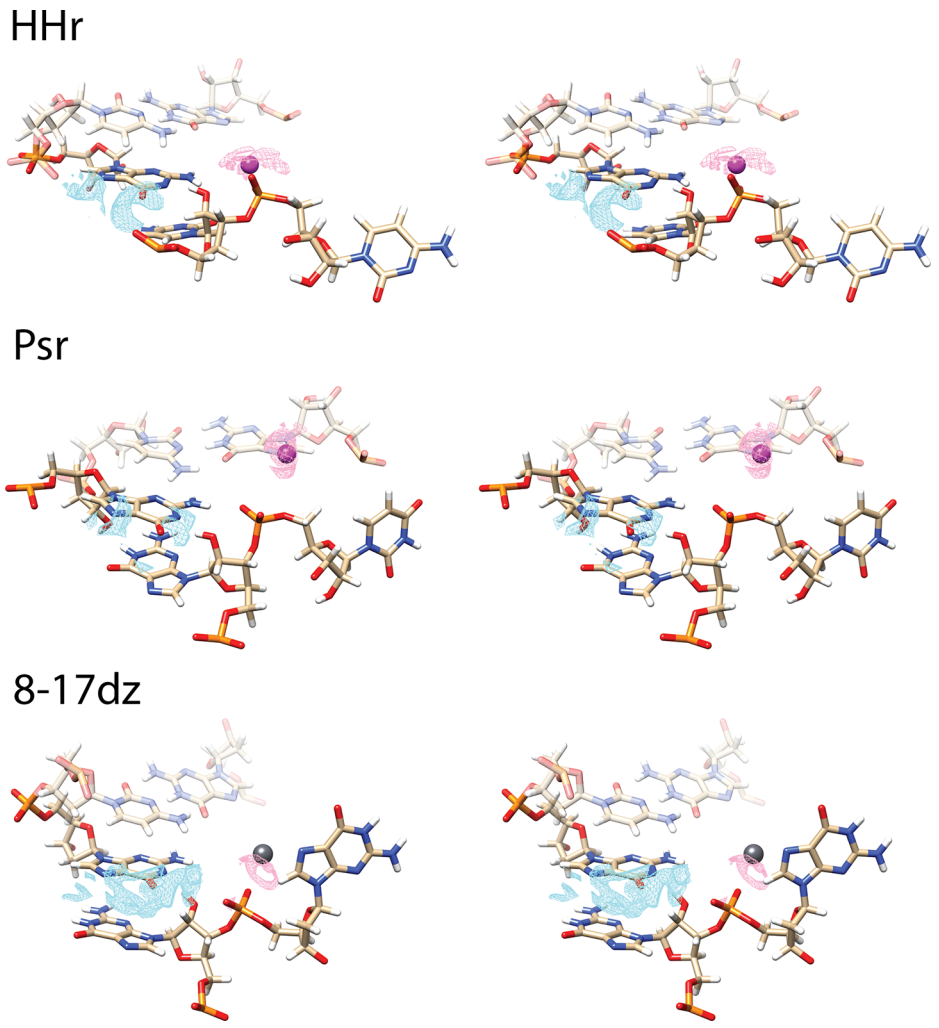

Figure 3. Active state metal ion binding isodensity contours for Na^+ around general base O6 and Mg^{2+} around NPO and L-pocket:O6 in HHr, Psr, and 8−17dz predicted by 3D-RISM. Mg^{2+} (magenta) and Na^+ (cyan) binding densities are calculated for the active states of the systems in the absence of explicit solvent and ions. The contour levels depicted are top 30%, 21.8%, and 30.9% for Mg^{2+} and top 18.3%, 19.4%, and 13.1% for Na^+ within 3 Å of corresponding ion interaction sites in HHr, Psr, and 8−17dz, respectively. Structures are depicted in parallel stereo.

predicted for these active states looking to answer the questions: (1) Where does 3D-RISM predict the Mg^{2+} ion will bind in the active site? (2) What is the local Na^+ ion distribution around the general base Hoogsteen edge?

As mentioned previously, HHr, Psr, and 8−17dz fall in the G+M category for RNA-cleaving nucleic acid enzymes, where the acid step depends on a divalent metal ion.[25,29] In crystal structures of HHr, Psr, and 8−17dz oftentimes the divalent metal ion is resolved to be bound at the Hoogsteen edge of the L-pocket guanine. The active state position of these metal ions, however, varies between the different systems. While HHr was shown to have direct coordination to pro-R_P (position corresponding to the *R* configuration of the planar pro-chiral center in accord with the IUPAC/Cahn-Ingold-Prelog stereo-descriptors) nonbridging phosphate oxygen (NPO),[26,68,69] Psr results suggest indirect coordination to pro-R_P and direct coordination to the L-pocket (G33) N7.[44,49] Divalent metal ion positioning in 8−17dz, however, has not yet been conclusively established. Measured pH-rate profiles[70] suggest a metal ion coordinated water to be acting as the acid. The crystal structure[51] and the dynamic studies of the active state[46] offer different binding modes in terms of pro-R_P coordination, however both still have the divalent metal ion at solvent separation from the O5′ leaving group allowing a coordinating water to act as the acid and therefore supporting these pH-rate results.

Figure 3 shows the Mg^{2+} ion densities (pink mesh) within 3 Å of pro-R_P and L-pocket:N7 calculated using 3D-RISM, depicted on the active state structures obtained from MD simulations for each system. The position of the divalent metal ions (Mg^{2+} for HHr and Psr, and Pb^{2+} for 8−17dz) are also shown to highlight the overlap between simulation and 3D-RISM calculations. The metal ion binding modes from MD simulation results have been supported by structural and biochemical experiments in each case. There is a very high overlap between the predicted Mg^{2+} densities and the experimentally/theoretically derived position of the divalent metal in all systems. Calculations predict a lower Mg^{2+} density at the nearby alternative binding site (L-pocket Hoogsteen edge O6/N7 for HHr and 8−17dz; and pro-R_P for Psr), the density for which are not apparent in the figures as they fall below the isocontour threshold values. This suggests that both binding sites are accessible, but the preferred Mg^{2+} binding mode is that indicated by the active state shown in the figure. In each case, the Mg^{2+} binding mode involved direct or indirect coordination with the NPO of the scissile phosphate

https://doi.org/10.1021/acs.jpcb.2c03727
J. Phys. Chem. B 2022, 126, 5982−5990

where it is positioned to provide direct electrostatic (Lewis acid) stabilization of the dianionic transition state and assist in leaving group departure (general acid catalysis) either via direct coordination or pK_a tuning of a coordinated water (Psr and 8−17dz) or the 2′OH of an active site residue that can then act as a general acid (G8 in HHr).

Similar to Mg^{2+}, we calculated Na^+ densities using 3D-RISM. Figure 3 blue mesh shows the calculated densities within 3 Å of N7 or O6 of general base guanine in each system. All systems have significant densities (>top 20% of density) around the Hoogsteen edge of the general base guanine, which is positioned to be exposed to the solvent. These results are consistent with the supposition that these nucleic acid enzymes create an electrostatically strained active site that can recruit a threshold amount of cationic charge from solution to assist in catalysis.[69]

pK_a Tuning of the General Base by Diffuse Territorial Na^+ Binding in G+M Nucleic Acid Enzymes. In all G+M systems the general base guanine is positioned with its Hoogsteen edge pointing toward solution.[29] Previous work on HHr has shown the effects of the metal ion binding at O6 of general base guanine (GB:O6) and how this is a mechanism used by the enzyme to tune its pK_a.[43,71,72] As shown by 3D-RISM predictions, HHr, Psr, and 8−17dz all exhibit enhanced recruitment of Na^+ density at the Hoogsteen edge of the general base guanine residue. These ions, if preferentially bound to the O6 position, would stabilize the N1-deprotonated (that is, anionic "activated") form required to extract the nucleophile proton for catalysis. This would serve to lower the guanine pK_a, enabling the activated general base (GB^-) to be more highly occupied at near-physiological pH. This pK_a-tuning of the general base by territorial binding of Na^+ ions is an important catalytic device employed by these enzymes.

We further investigated this behavior using MD simulations in an explicit solvent environment. Each system was simulated in its active and standard state for five independent 100 ns production runs (after discarding initial equilibration stages), yielding a total 500 ns of trajectories for analysis. The Na^+ ion distributions around O6 of every guanine within the systems were obtained along with running coordination numbers. Figure 4 shows the radial distribution functions and running coordination numbers for general base (GB) guanine in active (cyan) and standard (blue) state and the average values for all the remaining guanines along with their standard deviation. For all systems, the first peak for the general base guanine, especially in the active state, is statistically significantly greater than the average distribution and the standard deviation envelop. This indicates that the general base guanine has considerably greater directly bound Na^+ ion occupancy than the average.

Comparison of the Na^+ ion distribution functions for the activated general base (GB^-) leads to a more complicated situation. The activated general base guanine has the N1 position deprotonated, and through resonance stabilization, the excess negative charge is delocalized between the N1 and O6 positions.[43] As a general electrostatic consequence, there is more negative charge at the O6 position, and greater accumulation of Na^+ ion density. However, as the deprotonation causes a hydrogen bond donating group at N1 to be replaced by a hydrogen bond acceptor, there are local conformational changes that occur, making the interpretation of the distribution functions slightly more complicated in some

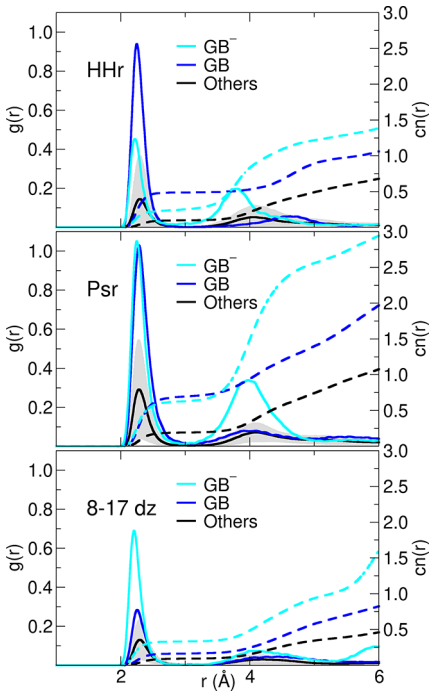

Figure 4. Radial distribution functions (RDFs), g(r), and running coordination number, cn(r), of Na^+ ions around O6 oxygens of guanines in standard and active states of HHr, Psr, and 8−17dz. RDFs are shown in solid lines, and cn in dashed lines. General base guanine values (HHR:G12, Psr:G40 and 8−17dz:G13) are shown in blue for standard state (GB), and in cyan for the active state (GB^-). Averages of all the other guanines (black line with the standard deviation shown as gray shaded area) were essentially the same for the two states and only the standard state is reported to avoid crowding the figure. Each set is calculated from 5 independent simulations totaling 500 ns.

cases. In the case of 8−17dz (bottom panel Figure 4), the GB^- distribution has a higher first peak, indicating the intuitive result that there is greater accumulation of Na^+ ions directly coordinating the O6. On the other hand, in the cases of Psr and HHr (middle and top panels Figure 4, respectively), the GB^- distribution has a first peak that is roughly the same (Psr) and lower (HHr) than that of the corresponding GB simulation. Upon inspection of the HHr trajectories, we saw a structural change take place going from the standard to the active state that restricts the solvent exposure of HHr general base (G12) O6. The NPO of the N-1 (C17) residue, shifts closer in toward G12:O6, yielding an average distance of 4.2 Å between the two oxygens, oftentimes bridged by a water molecule. A similar shift was also seen in the crystal structures obtained at various pH values (pH 5 and 8 structures corresponding to 6.4 and 5.6 Å, respectively)[71] and the transition state mimicking vanadate structure[72] (4.4 Å), consistently suggesting that in its active state C17 NPO of HHr shifts closer to the general base.

Nonetheless, in all cases the total number of ions (directly bound and territorially bound) increases substantially upon deprotonation of the general base. The directly bound ions are indicated by the first peak of the radial distribution function, whereas territorially bound ions arise mainly from the second peak. the running coordination number, cn(r), tracks the accumulation of both. As indicated in Figure 4, beyond 4 Å the coordination number around O6 of the general base is substantially greater in the GB^- simulation than in the GB

https://doi.org/10.1021/acs.jpcb.2c03727
J. Phys. Chem. B 2022, 126, 5982−5990

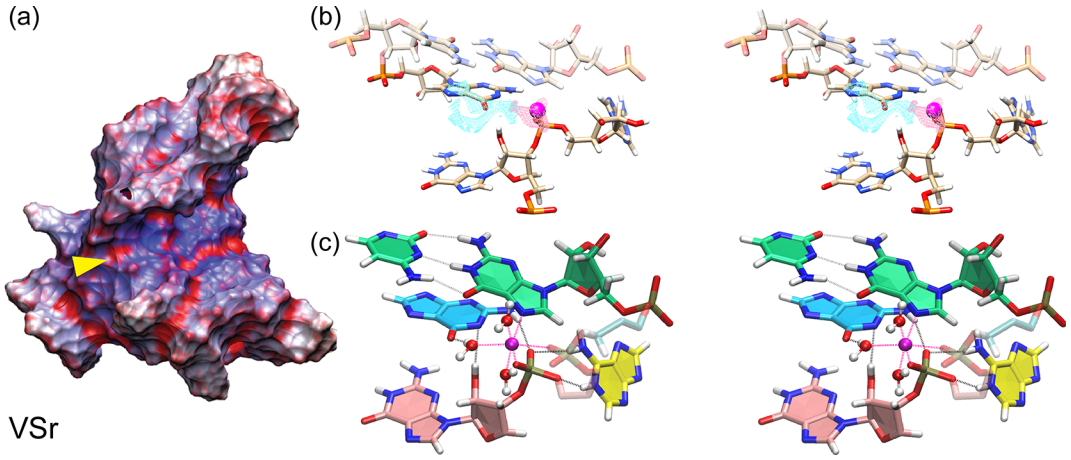

Figure 5. Electrostatics analysis helped identify an active site metal ion in VSr. (a) Electrostatic potential surface projected onto the molecular surface, coloring scheme same as Figure 2. (b) Metal ion binding isodensity contours calculated by 3D-RISM, in parallel stereo. Coloring scheme same as Figure 3, top 30% for Mg^{2+} and 20% for Na^{+} isodensity contours are depicted. (c) Active state structure from dynamics in explicit solvent, in parallel stereo. General base (G638, blue), general acid (A756, yellow), N-1 and scissile phosphate (G620, pink), L-pocket G623-C637, Mg^{2+} (magenta) along with coordinating waters (shown as CPK) are shown. Mg^{2+} coordinations are shown in magenta, and reaction related hydrogen bonds are in black dashed lines. Mg^{2+} coordinates pro-S_P of scissile phosphate, A622:pro-R_P, G623:O6 and 3 waters, one of which hydrogen bonds to general base G638:O6.

simulation, indicating greater association of Na^{+} ion density that occurs upon deprotonation of the general base, as would be required for tuning of the pK_a.

Functional Active Site Divalent Metal Ion Predicted for VSr, an Archetype G+A Ribozyme. Varkud Satellite virus ribozyme (VSr) is an archetype member of the G+A class.[25,73] Recently, several crystal structures of VSr became available,[50,74] and in none of them was there observed a divalent metal ion in the active site, suggesting there was not a functional role for such an ion. We carried out the same set of Poisson−Boltzmann, 3D-RISM electrostatics, and solvation model calculations for VSr. These are summarized in Figure 5.

The PBSA EPS indicates a local electronegative hotspot at the VSr active site (Figure 5a). 3D-RISM calculations show a highly localized Mg^{2+} isodensity around the pro-S_P (oxygen corresponding to the *S* configuration of the planar pro-chiral center) of the scissile phosphate (magenta mesh, Figure 5b), as well as significant nearby Na^{+} density around general base guanine O6 and N7 positions (blue mesh), which is consistent with all the G+M systems above. MD simulations performed in the absence of an active site Mg^{2+} ion (as indicated by the available crystal structures) did not produce an active state dynamical ensemble where the general base (G638) was poised to activate the nucleophile by abstracting the O2′ proton.[32] In fact, these simulations indicated that the general base was disordered, unlike the situation in the HHr, Psr, and 8−17dz, where this residue was anchored by a noncanonical base pair with the sugar edge. However, placement of a Mg^{2+} ion at the 3D-RISM predicted site enabled formation of an outer-sphere interaction with the G638:O6 (Figure 5c) that not only served to anchor the residue in position to abstract the nucleophile proton, but also tune the pK_a of the general base through a very strong hydrogen bond with the polarized water coordinated to the Mg^{2+} ion.

In a tour de force experimental/theoretical study,[32] the predicted Mg^{2+} binding site was verified experimentally through phosphorothioate/metal rescue experiments, enabling a comprehensive computational enzymology approach to be taken to gain deep insight into the catalytic mechanism. This insight led to the development of a L-platform/L-scaffold framework for nucleic acid enzyme design[29] (Figure 1a), whereby two key new elements to the L-platform motif originally described by Suslov and co-workers[74] were identified: the "L-anchor" (often a conserved adenine residue) that enables proper positioning of the general base through interactions with its sugar edge, and the "L-pocket" residue, a conserved guanine, that along with one or more phosphates in the active site, forms a functionally important divalent metal ion binding site. This L-pocket guanine is a conserved feature in all currently known G+M nucleic acid enzymes that use a divalent metal ion to assist in general acid catalysis. VSr appears thus far to be unique in utilizing the L-pocket and divalent metal ion as an L-anchor, and instead employs a conserved adenine residue as the general acid. This illustration showcases the immense importance of electrostatic interactions in the designs of nucleic acid enzymes.

Complementary Insight Gained from PB, 3D-RISM, and MD Methods. In this paper, we apply a hierarchy of methods to analyze electrostatic features and their implications to ion binding and catalysis for a set of metal-dependent nucleic acid enzymes. Poisson−Boltzmann calculations[33−37] treat the solvent as a continuous isotropic polarizable dielectric medium, with the effect of ions included through a Boltzmann term outside of an ion-excluding volume. As this is a continuum solvation theory, PB calculations provide an intuitive picture of general electrostatic features, including the electrostatic potential surface around the macromolecular solute (in this case the RNA or DNA enzymes) in a fixed (static) configuration. What the theory does not provide, however, is an accurate description of the solvent structure. 3D-RISM calculations, on the other hand, are a form of molecular solvation theory[38] that treats solvent−solute and solvent−solvent interactions through explicit solvent models and operates directly on the solvent distributions rather than individual molecules as in molecular dynamics. This enables an accurate representation of the solvent structure and thermodynamic properties to be obtained, including the characterization of territorial and site-specific ion binding[9] which can be

https://doi.org/10.1021/acs.jpcb.2c03727
J. Phys. Chem. B 2022, 126, 5982−5990

extremely challenging for MD simulations due to the time scales required to achieve convergence of the ion distributions and to overcome barriers to changes in coordination environment. A limitation of 3D-RISM is that it does not provide information about dynamics, and is much more computationally costly than a routine PB calculation, limiting its practical application to a relatively small number of solute configurations. Molecular dynamics simulations,[41,42] however, are able to generate large conformational ensembles from which detailed information about dynamical fluctuations of both solute and solvent can be derived. Hence, each one of these computational methods (PB, 3D-RISM, and MD) has advantages and disadvantages, and collectively provide a wealth of complementary information at different levels of resolution that enable new insights to be gained into RNA and DNA catalysis.

CONCLUSIONS

Electrostatics are central to the structure and function of nucleic acid enzymes, which fold into electrostatically strained 3D structures. Using a hierarchy of methods we extracted electrostatic features common to the active sites of HHr, Psr, and 8−17dz at multiple resolutions. Poison-Boltzmann calculations revealed the solvent exposed active sites are hotspots of negative electrostatic potential. 3D-RISM calculations predicted divalent metal ion binding sites are site-specific and overlap well with the active state positioning of the divalent metal ions obtained dynamically from MD simulations. 3D-RISM calculations similarly predicted high density for territorial binding of monovalent ions at the Hoogsteen edge (N7 and O6 positions) of the general base guanine, which were also explicitly shown by radial distribution of Na^+ obtained from MD simulations in explicit solvent. We showed that these general features enabled the prediction of functional divalent metal ion binding in the active site of VSr, which was not observed crystallographically, but was verified experimentally.[32] In this way, we show that nucleic acid electrostatics play an essential role in the recruitment of monovalent and divalent metal ions to the active sites of G+M nucleic acid enzymes and VSr, and that both site-specific and territorial binding are important for catalytic function. The results obtained here suggest that the combination of Poisson−Boltzmann and 3D-RISM calculations, along with molecular simulations, presents a promising approach to identify metal ion binding sites that may aid in the interpretation of structural NMR, X-ray crystallographic and cryo-EM data, and have wide application to other functional RNA and DNA systems.

AUTHOR INFORMATION

Corresponding Author

Darrin M. York − *Laboratory for Biomolecular Simulation Research, Institute for Quantitative Biomedicine and Department of Chemistry and Chemical Biology, Rutgers University, Piscataway, New Jersey 08854, United States;* orcid.org/0000-0002-9193-7055; Email: Darrin.York@rutgers.edu

Authors

Şölen Ekesan − *Laboratory for Biomolecular Simulation Research, Institute for Quantitative Biomedicine and Department of Chemistry and Chemical Biology, Rutgers University, Piscataway, New Jersey 08854, United States;* orcid.org/0000-0002-5598-5754

Erika McCarthy − *Laboratory for Biomolecular Simulation Research, Institute for Quantitative Biomedicine and Department of Chemistry and Chemical Biology, Rutgers University, Piscataway, New Jersey 08854, United States;* orcid.org/0000-0001-8089-0207

David A. Case − *Laboratory for Biomolecular Simulation Research, Institute for Quantitative Biomedicine and Department of Chemistry and Chemical Biology, Rutgers University, Piscataway, New Jersey 08854, United States;* orcid.org/0000-0003-2314-2346

Complete contact information is available at: https://pubs.acs.org/10.1021/acs.jpcb.2c03727

Notes

The authors declare no competing financial interest.

ACKNOWLEDGMENTS

The authors are grateful for financial support provided by the National Institutes of Health (No. GM62248 to DMY), and to Alan Grossman for providing early stage seed support for our research through the Grossman Innovation Prize. Computational resources that have contributed to the research results reported within this work were provided by the Office of Advanced Research Computing (OARC) at Rutgers, The State University of New Jersey, and the Extreme Science and Engineering Discovery Environment (XSEDE), which is supported by National Science Foundation Grant ACI-1548562 (specifically, the resources EXPANSE and COMET at SDSC through allocation TG-CHE190067), and the Texas Advanced Computing Center (TACC, http://www.tacc.utexas.edu) at The University of Texas at Austin, specifically the Frontera Supercomputer.

REFERENCES

(1) Kruger, K.; Grabowski, P. J.; Zaug, A. J.; Sands, J.; Gottschling, D. E.; Cech, T. R. Self-splicing RNA: autoexcision and autocyclisation of the ribosomal RNA intervening sequence of *Tetrahymena*. *Cell* **1982**, *31*, 147−157.

(2) Breaker, R. R.; Joyce, G. F. A DNA enzyme that cleaves RNA. *Chem. Biol.* **1994**, *1*, 223−229.

(3) Chin, K.; Sharp, K. A.; Honig, B.; Pyle, A. M. Calculating the electrostatic properties of RNA provides new insights into molecular interactions and function. *Nat. Struct. Biol.* **1999**, *6*, 1055−1061.

(4) Draper, D. E. A guide to ions and RNA structure. *RNA* **2004**, *10*, 335−343.

(5) Bloomfield, V. A.; Crothers, D. M.; Tinoco, Jr., I. *Nucleic Acids: Structures, Properties, and Functions*; University Science Books: Sausalito, CA, 2000.

(6) Bai, Y.; Greenfeld, M.; Travers, K. J.; Chu, V. B.; Lipfert, J.; Doniach, S.; Herschlag, D. Quantitative and comprehensive decomposition of the ion atmosphere around nucleic acids. *J. Am. Chem. Soc.* **2007**, *129*, 14981−14988.

(7) Lipfert, J.; Doniach, S.; Das, R.; Herschlag, D. Understanding Nucleic Acid-Ion Interactions. *Annu. Rev. Biochem.* **2014**, *83*, 813−841.

(8) Giambasu, G. M.; Gebala, M. K.; Panteva, M. T.; Luchko, T.; Case, D. A.; York, D. M. Competitive Interaction of Monovalent Cations With DNA From 3D-RISM. *Nucleic Acids Res.* **2015**, *43*, 8405−8415.

(9) Giambaşu, G. M.; Case, D. A.; York, D. M. Predicting Site-Binding Modes of Ions and Water to Nucleic Acids Using Molecular Solvation Theory. *J. Am. Chem. Soc.* **2019**, *141*, 2435−2445.

(10) Bevilacqua, P. C.; Harris, M. E.; Piccirilli, J. A.; Gaines, C.; Ganguly, A.; Kostenbader, K.; Ekesan, Ş.; York, D. M. An Ontology

for Facilitating Discussion of Catalytic Strategies of RNA-Cleaving Enzymes. *ACS Chem. Biol.* **2019**, *14*, 1068−1076.
(11) Lilley, D. M. Structures of helical junctions in nucleic acids. *Q. Rev. Biophys.* **2000**, *33*, 109−159.
(12) DeRose, V. J.; Yglesias, M. V. Metal Ion Interactions With DNA, RNA, and Nucleic Acid Enzymes. In *Comprehensive Coordination Chemistry III*; Constable, E. C., Parkin, G., Que, Jr, L., Eds.; Elsevier: Oxford, 2021; Vol. *8*; pp 968−993.
(13) Chu, V. B.; Bai, Y.; Lipfert, J.; Herschlag, D.; Doniach, S. A repulsive field: advances in the electrostatics of the ion atmosphere. *Curr. Opin. Chem. Biol.* **2008**, *12*, 619−625.
(14) Ma, C. Y.; Pezzotti, S.; Schwaab, G.; Gebala, M.; Herschlag, D.; Havenith, M. Cation enrichment in the ion atmosphere is promoted by local hydration of DNA. *Phys. Chem. Chem. Phys.* **2021**, *23*, 23203−23213.
(15) Yu, B.; Iwahara, J. Experimental approaches for investigating ion atmospheres around nucleic acids and proteins. *Comput. Struct. Biotechnol. J.* **2021**, *19*, 2279−2285.
(16) Gebala, M.; Giambasu, G. M.; Lipfert, J.; Bisaria, N.; Bonilla, S.; Li, G.; York, D. M.; Herschlag, D. Cation-Anion Interactions within the Nucleic Acid Ion Atmosphere Revealed by Ion Counting. *J. Am. Chem. Soc.* **2015**, *137*, 14705−14715.
(17) Gebala, M.; Bonilla, S.; Bisaria, N.; Herschlag, D. Does Cation Size Affect Occupancy and Electrostatic Screening of the Nucleic Acid Ion Atmosphere? *J. Am. Chem. Soc.* **2016**, *138*, 10925−10934.
(18) Gebala, M.; Herschlag, D. Quantitative Studies of an RNA Duplex Electrostatics by Ion Counting. *Biophys. J.* **2019**, *117*, 1116−1124.
(19) Das, R.; Mills, T. T.; Kwok, L. W.; Maskel, G. S.; Millett, I. S.; Doniach, S.; Finkelstein, K. D.; Herschlag, D.; Pollack, L. Counterion Distribution around DNA Probed by Solution X-Ray Scattering. *Phys. Rev. Lett.* **2003**, *90*, 188103.
(20) Andresen, K.; Das, R.; Park, H. Y.; Smith, H.; Kwok, L. W.; Lamb, J. S.; Kirkland, E. J.; Herschlag, D.; Finkelstein, K. D.; Pollack, L. Spatial Distribution of Competing Ions around DNA in Solution. *Phys. Rev. Lett.* **2004**, *93*, 248103.
(21) He, W.; Chen, Y.-L.; Pollack, L.; Kirmizialtin, S. The structural plasticity of nucleic acid duplexes revealed by WAXS and MD. *Sci. Adv.* **2021**, *7*, 6106.
(22) Pabit, S. A.; Katz, A. M.; Tolokh, I. S.; Drozdetski, A.; Baker, N.; Onufriev, A. V.; Pollack, L. Understanding nucleic acid structural changes by comparing wide-angle x-ray scattering (WAXS) experiments to molecular dynamics simulations. *J. Chem. Phys.* **2016**, *144*, 205102.
(23) Yu, B.; Pletka, C. C.; Iwahara, J. Quantifying and visualizing weak interactions between anions and proteins. *Proc. Natl. Acad. Sci. U.S.A.* **2021**, *118*, 2015879118.
(24) Pletka, C. C.; Nepravishta, R.; Iwahara, J. Detecting Counterion Dynamics in DNA−Protein Association. *Angew. Chem. Engl.* **2020**, *59*, 1465−1468.
(25) Lilley, D. M. J. Classification of the nucleolytic ribozymes based upon catalytic mechanism. *F1000 Res.* **2019**, *8*, 1462.
(26) Ward, W. L.; Plakos, K.; DeRose, V. J. Nucleic acid catalysis: metals, nucleobases, and other cofactors. *Chem. Rev.* **2014**, *114*, 4318−4342.
(27) Hollenstein, M. DNA Catalysis: The Chemical Repertoire of DNAzymes. *Molecules* **2015**, *20*, 20777−20804.
(28) Silverman, S. K. Catalytic DNA: Scope, Applications, and Biochemistry of Deoxyribozymes. *Trends Biochem. Sci.* **2016**, *41*, 595−609.
(29) Gaines, C. S.; Piccirilli, J. A.; York, D. M. The L-platform/L-scaffold framework: a blueprint for RNA-cleaving nucleic acid enzyme design. *RNA* **2020**, *26*, 111−125.
(30) Kuimelis, R. G.; McLaughlin, L. W. Mechanisms of Ribozyme-Mediated RNA Cleavage. *Chem. Rev.* **1998**, *98*, 1027−1044.
(31) Bashkin, J. K. Introduction to RNA/DNA Cleavage. *Chem. Rev.* **1998**, *98*, 937−938.
(32) Ganguly, A.; Weissman, B. P.; Giese, T. J.; Li, N.-S.; Hoshika, S.; Rao, S.; Benner, S. A.; Piccirilli, J. A.; York, D. M. Confluence of theory and experiment reveals the catalytic mechanism of the Varkud satellite ribozyme. *Nat. Chem.* **2020**, *12*, 193−201.
(33) Gilson, M. K.; Sharp, K. A.; Honig, B. H. Calculating the electrostatic potential of molecules in solution: method and error assessment. *J. Comput. Chem.* **1988**, *9*, 327−335.
(34) Gilson, M. K.; Honig, B. Calculation of the Total Electrostatic Energy of a Macromolecular System: Solvation Energies, Binding Energies, and Conformational Analysis. *Proteins* **1988**, *4*, 7−18.
(35) Luo, R.; David, L.; Gilson, M. K. Accelerated Poisson-Boltzmann calculations for static and dynamic systems. *J. Comput. Chem.* **2002**, *23*, 1244−1253.
(36) Wang, J.; Luo, R. Assessment of linear finite-difference Poisson-Boltzmann solvers. *J. Comput. Chem.* **2010**, *31*, 1689−1698.
(37) Cai, Q.; Hsieh, M.-J.; Wang, J.; Luo, R. Performance of Nonlinear Finite-Difference Poisson − Boltzmann Solvers. *J. Chem. Theory Comput.* **2010**, *6*, 203−211.
(38) Kovalenko, A. Three-dimensional RISM Theory for Molecular Liquids and Solid-Liquid Interface. In *Molecular Theory of Solvation*; Hirata, F., Ed.; Springer: Amsterdam, 2003; pp 169−275.
(39) Luchko, T.; Gusarov, S.; Roe, D. R.; Simmerling, C.; Case, D. A.; Tuszynski, J.; Kovalenko, A. Three-dimensional molecular theory of solvation coupled with molecular dynamics in AMBER. *J. Chem. Theory Comput.* **2010**, *6*, 607−624.
(40) Genheden, S.; Luchko, T.; Gusarov, S.; Kovalenko, A.; Ryde, U. An MM/3D-RISM Approach for Ligand Binding Affinities. *J. Phys. Chem. B* **2010**, *114*, 8505−8516.
(41) McCammon, J. A.; Harvey, S. C. *Dynamics of Proteins and Nucleic Acids*; Cambridge University Press: Cambridge, 1987.
(42) Karplus, M. Molecular dynamics simulations of biomolecules. *Acc. Chem. Res.* **2002**, *35*, 321−323.
(43) Chen, H.; Giese, T. J.; Golden, B. L.; York, D. M. Divalent Metal Ion Activation of a Guanine General Base in the Hammerhead Ribozyme: Insights from Molecular Simulations. *Biochemistry* **2017**, *56*, 2985−2994.
(44) Kostenbader, K.; York, D. M. Molecular simulations of the pistol ribozyme: unifying the interpretation of experimental data and establishing functional links with the hammerhead ribozyme. *RNA* **2019**, *25*, 1439−1456.
(45) Ekesan, Ş.; York, D. M. Who stole the proton? Suspect general base guanine found with a smoking gun in the pistol ribozyme. *Org. Biomol. Chem.* **2022**, DOI: 10.1039/D2OB00234E.
(46) Ekesan, Ş.; York, D. M. Dynamical ensemble of the active state and transition state mimic for the RNA-cleaving 8−17 DNAzyme in solution. *Nucleic Acids Res.* **2019**, *47*, 10282−10295.
(47) Ganguly, A.; Weissman, B. P.; Piccirilli, J. A.; York, D. M. Evidence for a Catalytic Strategy to Promote Nucleophile Activation in Metal-Dependent RNA-Cleaving Ribozymes and 8−17 DNAzyme. *ACS Catal.* **2019**, *9*, 10612−10617.
(48) Martick, M.; Lee, T.-S.; York, D. M.; Scott, W. G. Solvent structure and hammerhead ribozyme catalysis. *Chem. Biol.* **2008**, *15*, 332−342.
(49) Wilson, T. J.; Liu, Y.; Li, N. S.; Dai, Q.; Piccirilli, J. A.; Lilley, D. M. Comparison of the structures and mechanisms of the pistol and hammerhead ribozymes. *J. Am. Chem. Soc.* **2019**, *141*, 7865−7875.
(50) DasGupta, S.; Suslov, N. B.; Piccirilli, J. A. Structural Basis for Substrate Helix Remodeling and Cleavage Loop Activation in the Varkud Satellite Ribozyme. *J. Am. Chem. Soc.* **2017**, *139*, 9591−9597.
(51) Liu, H.; Yu, X.; Chen, Y.; Zhang, J.; Wu, B.; Zheng, L.; Haruehanroengra, P.; Wang, R.; Li, S.; Lin, J.; Li, J.; Sheng, J.; Huang, Z.; Ma, J.; Gan, J.; et al. Crystal Structure of an RNA-Cleaving DNAzyme. *Nat. Commun.* **2017**, *8*, 2006−2015.
(52) Case, D. A.; Belfon, K.; Ben-Shalom, I. Y.; Brozell, S. R.; Cerutti, D. S.; Cheatham, III, T. E.; Cruzeiro, V. W. D.; Darden, T. A.; Duke, R. E.; Giambasu, G. et al. *AMBER 20*; University of California: San Francisco, CA, 2020.
(53) Pérez, A.; Marchán, I.; Svozil, D.; Sponer, J.; Cheatham, T. E., III; Laughton, C. A.; Orozco, M. Refinement of the AMBER force field for nucleic acids: Improving the description of α/γ conformers. *Biophys. J.* **2007**, *92*, 3817−3829.

(54) Zgarbová, M.; Otyepka, M.; Šponer, J.; Mládek, A.; Banáš, P.; Cheatham, T. E., III; Jurečka, P. Refinement of the Cornell et al. nucleic acids force field based on reference quantum chemical calculations of glycosidic torsion profiles. *J. Chem. Theory Comput.* **2011**, *7*, 2886−2902.
(55) Zgarbova, M.; Sponer, J.; Otyepka, M.; Cheatham, T. E., III; Galindo-Murillo, R.; Jurecka, P. Refinement of the sugar-phosphate backbone torsion beta for AMBER Force Fields improves the description of Z- and B-DNA. *J. Chem. Theory Comput.* **2015**, *11*, 5723−5736.
(56) Horn, H. W.; Swope, W. C.; Pitera, J. W.; Madura, J. D.; Dick, T. J.; Hura, G. L.; Head-Gordon, T. Development of an improved four-site water model for biomolecular simulations: TIP4P-Ew. *J. Chem. Phys.* **2004**, *120*, 9665−9678.
(57) Joung, I. S.; Cheatham, T. E., III Determination of alkali and halide monovalent ion parameters for use in explicitly solvated biomolecular simulations. *J. Phys. Chem. B* **2008**, *112*, 9020−9041.
(58) Li, P.; Merz, K. M., Jr. Taking into account the ion-induced dipole interaction in the nonbonded model of ions. *J. Chem. Theory Comput.* **2014**, *10*, 289−297.
(59) Panteva, M. T.; Giambaşu, G. M.; York, D. M. Comparison of structural, thermodynamic, kinetic and mass transport properties of Mg^{2+} ion models commonly used in biomolecular simulations. *J. Comput. Chem.* **2015**, *36*, 970−982.
(60) Panteva, M. T.; Giambasu, G. M.; York, D. M. Force Field for Mg^{2+}, Mn^{2+}, Zn^{2+}, and Cd^{2+} Ions that have Balanced Interactions with Nucleic Acids. *J. Phys. Chem. B* **2015**, *119*, 15460−15470.
(61) Ditzler, M. A.; Otyepka, M.; Sponer, J.; Walter, N. G. Molecular dynamics and quantum mechanics of RNA: conformational and chemical change we can believe in. *Acc. Chem. Res.* **2010**, *43*, 40−47.
(62) Darden, T.; York, D.; Pedersen, L. Particle mesh Ewald: An N log(N) method for Ewald sums in large systems. *J. Chem. Phys.* **1993**, *98*, 10089−10092.
(63) Essmann, U.; Perera, L.; Berkowitz, M. L.; Darden, T.; Lee, H.; Pedersen, L. G. A smooth particle mesh Ewald method. *J. Chem. Phys.* **1995**, *103*, 8577−8593.
(64) Ryckaert, J. P.; Ciccotti, G.; Berendsen, H. J. C. Numerical Integration of the Cartesian Equations of Motion of a System with Constraints: Molecular Dynamics of n-Alkanes. *J. Comput. Phys.* **1977**, *23*, 327−341.
(65) Miyamoto, S.; Kollman, P. A. SETTLE: An analytic version of the SHAKE and RATTLE algorithms for rigid water models. *J. Comput. Chem.* **1992**, *13*, 952−962.
(66) Berendsen, H. J. C.; Grigera, J. R.; Straatsma, T. P. The Missing Term in Effective Pair Potentials. *J. Phys. Chem.* **1987**, *91*, 6269−6271.
(67) Roe, D. R.; Cheatham, T. E., III PTRAJ and CPPTRAJ: Software for Processing and Analysis of Molecular Dynamics Trajectory Data. *J. Chem. Theory Comput.* **2013**, *9*, 3084−3095.
(68) Lee, T.-S.; Silva López, C.; Giambaşu, G. M.; Martick, M.; Scott, W. G.; York, D. M. Role of Mg^{2+} in hammerhead ribozyme catalysis from molecular simulation. *J. Am. Chem. Soc.* **2008**, *130*, 3053−3064.
(69) Lee, T.-S.; Giambaşu, G. M.; Sosa, C. P.; Martick, M.; Scott, W. G.; York, D. M. Threshold Occupancy and Specific Cation Binding Modes in the Hammerhead Ribozyme Active Site are Required for Active Conformation. *J. Mol. Biol.* **2009**, *388*, 195−206.
(70) Cortés-Guajardo, C.; Rojas-Hernández, F.; Paillao-Bustos, R.; Cepeda-Plaza, M. Hydrated metal ion as a general acid in the catalytic mechanism of the 8−17 DNAzyme. *Org. Biomol. Chem.* **2021**, *19*, 5395−5402.
(71) Mir, A.; Chen, J.; Robinson, K.; Lendy, E.; Goodman, J.; Neau, D.; Golden, B. L. Two Divalent Metal Ions and Conformational Changes Play Roles in the Hammerhead Ribozyme Cleavage Reaction. *Biochemistry* **2015**, *54*, 6369−6381.
(72) Mir, A.; Golden, B. L. Two Active Site Divalent Ions in the Crystal Structure of the Hammerhead Ribozyme Bound to a Transition State Analogue. *Biochemistry* **2016**, *55*, 633−636.
(73) Lilley, D. M. J. The varkud satellite ribozyme. *RNA* **2004**, *10*, 151−158.
(74) Suslov, N. B.; DasGupta, S.; Huang, H.; Fuller, J. R.; Lilley, D. M. J.; Rice, P. A.; Piccirilli, J. A. Crystal Structure of the Varkud Satellite Ribozyme. *Nat. Chem. Biol.* **2015**, *11*, 840−846.

https://doi.org/10.1021/acs.jpcb.2c03727
J. Phys. Chem. B 2022, 126, 5982−5990